Article

Optimizing Micro-CT Resolution for Geothermal Reservoir Characterization in the Pannonian Basin

Rita Mwendia Njeru [1,2,*], Akhmad Sofyan [1,3], Matthias Halisch [4], Balázs Kóbor [1,5] and János Szanyi [1]

1   Department of Mineralogy, Geochemistry and Petrology, University of Szeged (SZTE), Egytem Str. 2, H-6722 Szeged, Hungary; civilpetro@gmail.com (A.S.); szanyi@iif.u-szeged.hu (J.S.); kobor.balazs@yahoo.com (B.K.)
2   Department of Physics, Faculty of Science, Egerton University, Egerton 536-20115, Kenya
3   Polytechnic of Energy and Mineral Akamigas, Ministry of Energy and Mineral Resources (KESDM), Cepu, Blora 58315, Central Java, Indonesia
4   Leibniz Institute for Applied Geophysics (LIAG), Department 5-Petrophysics & Borehole Geophysics, Stilleweg 2, GEOZentrum Hannover, D-30655 Hannover, Germany; matthias.halisch@leibniz-liag.de
5   Geothermal Energy Applied Research Center (GEAR), University of Szeged (SZTE), Dugonics Square 13, H-6722 Szeged, Hungary
*   Correspondence: mwenderita@gmail.com; Tel.: +36-205-357-431 or +254-728-348-560

Abstract: In the context of global efforts to transition toward renewable energy and reduce greenhouse gas emissions, geothermal energy is increasingly recognized as a viable and sustainable option. This paper presents a comprehensive assessment derived from a subset of a larger sample collection within the Dunántúli Group of the Pannonian Basin, Hungary, focusing on optimizing micro-computed tomography (μ-CT) resolution for analyzing pore structures in sandstone formations. By categorizing samples based on geological properties and selecting representatives from each group, the study integrates helium porosity and gas permeability measurements with μ-CT imaging at various resolutions (5 μm, 2 μm, and 1 μm). The findings reveal that μ-CT resolution significantly affects the discernibility and characterization of pore structures. Finer resolutions (2 μm and 1 μm) effectively uncovered interconnected pore networks in medium- to coarse-grained sandstones, suggesting favorable properties for geothermal applications. In contrast, fine-grained samples showed limitations in geothermal applicability at higher resolutions due to their compact nature and minimal pore connectivity, which could not be confidently imaged at 1 μm. Additionally, this study acknowledges the challenges in delineating the boundaries within the Dunántúli Group formations, which adds a layer of complexity to the characterization process. The research highlights the importance of aligning μ-CT findings with geological backgrounds and laboratory measurements for accurate pore structure interpretation in heterogeneous formations. By contributing vital petrophysical data for the Dunántúli Group and the Pannonian Basin, this study provides key insights for selecting appropriate μ-CT imaging resolutions to advance sustainable geothermal energy strategies in the region. The outcomes of this research form the basis for future studies aimed at developing experimental setups to investigate physical clogging and enhance geothermal exploitation methods, crucial for the sustainable development of geothermal resources in the Pannonian Basin.

Keywords: Dunántúli Group; geothermal energy; micro-CT imaging; resolution; sandstone

1. Introduction

The global energy crisis and escalating demand have intensified the search for sustainable solutions, with geothermal energy emerging as a key alternative [1,2]. This renewable energy source, which harnesses the Earth's inherent heat, offers a viable pathway for both electricity generation and heating applications, making a significant contribution to achieving net-zero emissions [1,3]. High-resolution μ-CT imaging has proven effective in identifying significant porosity and variable permeability in the Dunántúli Group (DG)

sandstones, essential for optimizing geothermal fluid injection and minimizing clogging risks [4]. In addition to providing continuous, reliable power, geothermal energy meets global environmental goals by operating without greenhouse gas emissions.

The geothermal potential in Europe, and especially in Hungary, is considerable. This potential, which is extensively documented in the Atlas of Geothermal Resources, is particularly pronounced in the sand and sandstone layers of the Pannonian Basin, which are characterized by their favorable porous and permeable properties [5–8]. In the Pannonian Basin, especially around the cities of Szentes and Szeged, the geothermal gradient ranges from 45 to 50 °C per 1000 m depth, providing favorable conditions for geothermal energy production. These gradients reflect significant geothermal anomalies that enhance the geothermal potential of the region [9]. Such anomalies are closely related to the geological and tectonic framework of the basin, which includes numerous faults and fractures. These structural features facilitate the movement of geothermal fluids, contribute to the formation of geothermal plumes, and influence the overall thermal characteristics of the region. This sets the stage for Hungary to capitalize on its geothermal potential to potentially meet national energy targets.

The focus of this study is the DG, a Miocene formation within the Pannonian Basin known for its sandstones, siltstones, and shales [9–12]. Despite its recognized potential for geothermal energy exploitation, limited public access to detailed data on the reservoir rock properties of Hungarian geothermal projects, particularly those within the DG, poses a challenge to a comprehensive understanding and optimization of these resources [10].

Extensive research in Hungary has investigated various dimensions of geothermal energy, including vapor–liquid equilibria, groundwater heat transport, and ground movements due to pore pressure fluctuations [2,13,14]. These studies highlight the critical need for accurate characterization of geothermal reservoirs in order to optimize energy extraction and effectively manage environmental impacts. A major challenge in this area is the efficient reinjection of spent fluids into geothermal reservoirs. The lack of detailed knowledge of micropathways within formations such as the DG often leads to clogging during reinjection processes, which has been documented in several Hungarian projects [10,11]. Addressing this issue requires an in-depth understanding of these micropaths in order to prevent operational inefficiencies and ensure sustainable resource management.

The μ-CT imaging method has emerged as a pivotal non-destructive technique in the analysis of geological formations, offering high-resolution insights into the pore structure of reservoir rocks [15]. This technique, as demonstrated in the work of [16] and further explored by Buday Bond and Hurter and Schellschmidt [5,17], allows for detailed assessments of porosity, permeability, and fluid flow characteristics that are vital for the management of both geothermal and hydrocarbon reservoir dynamics. Moreover, the authors of [18] have demonstrated the value of μ-CT in investigating tight turbidite sandstone formations, illustrating its versatility beyond geothermal contexts.

In order to address the gaps identified in previous studies, our research integrates helium porosity and permeability measurements with high-resolution μ-CT imaging in order to examine the DG samples at various resolutions. This approach not only addresses a significant research gap in Hungary but also provides a comprehensive assessment of the formation's suitability for geothermal energy exploitation. The integration of different resolutions in μ-CT imaging has the effect of enhancing our ability to analyze and visualize the complex pore structures within the DG, thereby setting a new precedent in the field of geothermal energy exploration in the region.

Recent advances in this field, as exemplified by the work of Xiong [19], who combined μ-CT data at different resolutions with numerical simulations, have highlighted the importance of resolution in accurately predicting petrophysical properties across complex reservoir rocks. These advances have significantly enhanced our understanding of the influence of resolution on the visualization and analysis of pore structures, contributing to the optimization of geothermal reservoir performance. This approach is analogous to that of [20], who employed both nano-CT and μ-CT to investigate multi-scale pore structures in

shale. They applied segmentation techniques to high-resolution µ-CT images in order to enhance the quantification and spatial distribution of pore networks.

In the Újfalu Formation within the DG, recent studies, particularly those conducted by Willems [10], have predominantly focused on the permeability and mineralogy. Our research represents a pioneering approach to a systematic comparative analysis across specific µ-CT imaging resolutions (5 µm, 2 µm, and 1 µm) with the objective of analyzing pore networks, porosity, and permeability in the DG sandstone. This resolution-specific analysis, hitherto not utilized in DG studies, offers novel insights into the intricate pore structures of geothermal reservoir rocks, thereby enhancing our comprehension and stewardship of these resources for the sustainable production of geothermal energy.

2. Materials and Methods

### 2.1. The Study Area and Sample Collection and Preparation

The Pannonian Basin, known for its extensive geothermal resources, is home to the Szentes geothermal field—a key site for geothermal energy in Hungary [21]. It is situated in the southern reaches of the Great Hungarian Plain in the northeastern section of the Makó–Hódmezővásárhely Trough. The area features a pre-Neogene basement that plunges to depths between 4500 and 5000 m. It experienced over 4000 m of sediment deposition during the Pannonian period, characterized by a shoaling-upward sequence influenced by the Alpine–Carpathian source [22]. This sequence includes five principal depositional environments ranging from coarse-grained basal turbidites to shallow lake and braided stream deposits [23]. Sand accumulation in the trough, influenced by climate and sediment supply, reached its peak during the early highstand aggradational stage [24]. As seen in the geological map in Figure 1, the Lower Pannonian formations comprising Algyő, Szolnok, and Endrőd formations, along with Tótkomlós marl, now part of the Alföld Group, and the Upper Pannonian formations encompassing the Zagyva and Újfalu formations, which are part of the Transdanubian Formation Group currently named the Dunántúli Group, reflect this complex stratigraphy [25].

In the Szentes Geothermal Field, within the DG, three aquifer layers are utilized, correlating with the depth and geological features reported by Bálint and Szanyi, and Koroncz [25,26]. Level A, the uppermost layer, includes wells in the Újfalu and Zagyva formations at depths of 1500–1800 m, characterized by an average permeability of 1500 mD. Level B, in the middle, encompasses wells between 1800 and 2000 m, mainly in the Újfalu Formation and partly in Zagyva, with a permeability of around 500 mD. This layer is the primary source of thermal water production. Level C, the deepest layer situated below 2000 m entirely in the Újfalu Formation, exhibits permeability between 1000 and 2000 mD [25]. The samples for this study were collected from a depth ranging between 1936 and 1960 m, placing them within Level B, the middle aquifer layer group of the DG.

In Figure 1, we present a detailed topographical map that shows the Szentes area within the broader landscape of the Pannonian Basin. This illustration pinpoints the geographical location where our samples were collected and where our research into the viability of geothermal energy unfolds. This area is key in improving our comprehension of the geothermal energy exploitation in this part of Central Europe. Its hydrothermally active fault network and zones of low electrical resistivity, combined with notable porosity and permeability, make it highly suitable for geothermal power and district heating [8].

Our study focused on the middle aquifer layer group of the DG at depths of 1800 to 2000 m. This layer is characterized by a moderate permeability of approximately 500 mD. Our study involved a strategic selection of core samples from a larger collection, where they were categorized into two based on specific geological properties like grain size and cementation. From these distinct categories, we chose two samples of each type for detailed analysis: Sample A, which is a more porous, medium- to coarse-grained sandstone, and Sample B, a denser, fine-grained sandstone with lower porosity and permeability. Type B sandstone represents a more compact form of sandstone with potentially higher clay

content. These samples, taken from depths between 1936 and 1960 m, fall within the essential depth range of the middle aquifer [25,26].
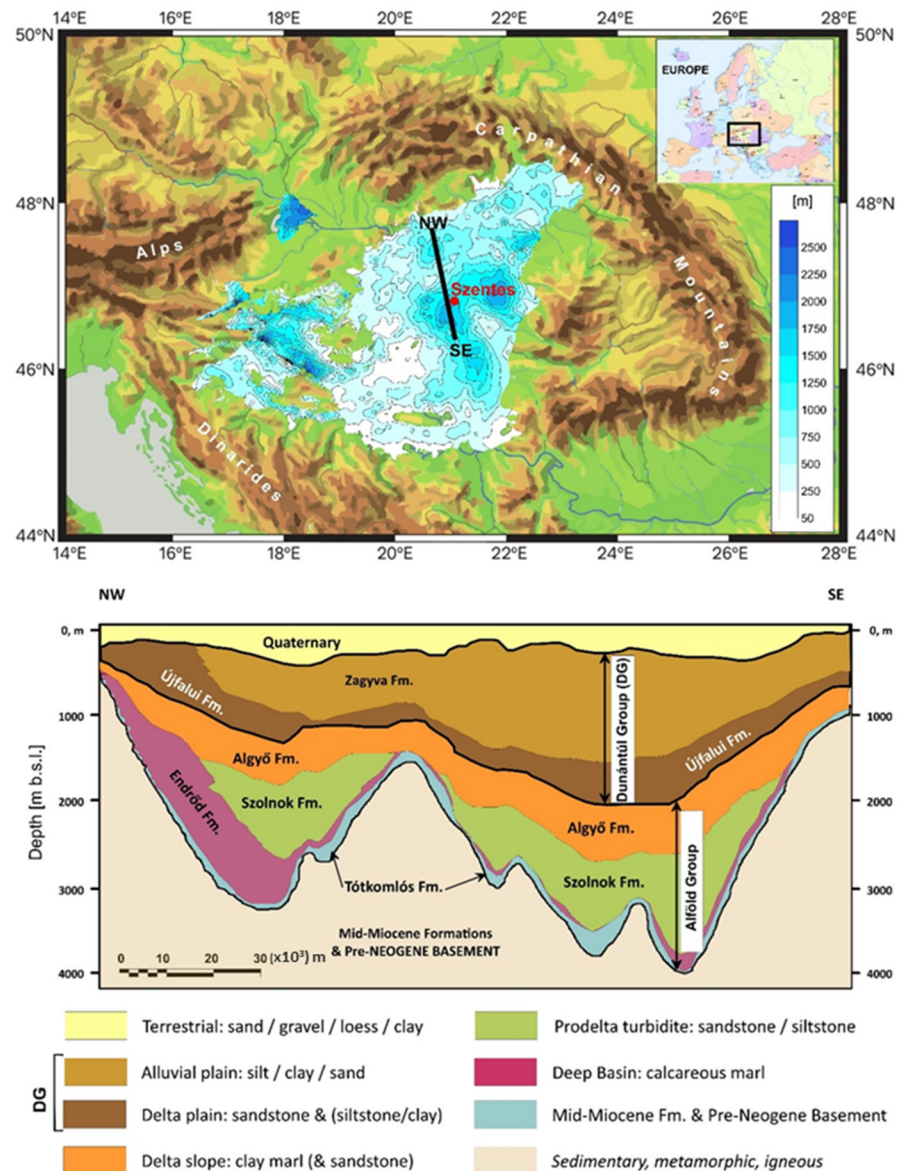
Figure 1. The thickness of the Dunántúl Group in the Carpathian Basin (above) and cross-section (below) of the Great Hungarian Plain sediments and stratigraphy in the late Miocene; the cross-section is shown as a black line in the above figure with the location of the study area indicated with a red dot (based on Geoconnect3D project and Almási and Szanyi [27]).

The selected samples underwent further preparations for our study. This involved drying for 24 h at a temperature of about 65 degrees to expel any moisture present. The samples first underwent a simple lab measurement for porosity and permeability to provide initial insights for the μ-CT investigations that were to follow. They were then prepared stepwise for high-resolution μ-CT scanning at various resolutions (5 μm, 2 μm, and 1 μm). These steps involved careful step-by-step size reduction in the samples, as will be explained in the respective sections, to ensure suitable size for the μ-CT scanning process while still representative of their original geological context. This meticulous preparation was critical in accurately assessing the pore structures of the samples, thereby contributing to a comprehensive understanding of their potential for geothermal energy exploitation.

### 2.2. Gas Porosity and Permeability Measurements

Core samples' selection and preparation were followed by an initial evaluation to deeply understand their porosity and permeability characteristics. Porosity measurements were carried out using a helium gas and a helium pycnometer. On the other hand, permeability measurements were made using nitrogen gas at steady-state flow and using a Hassler-type permeameter at Geochem Ltd. Kozarmisleny, Hungary. These gas measurements adhered to the standards set by the American Petroleum Institute [28]. This step utilized a total of four samples; two replicas from sample category A (A1 and A2) and two replicas from sample category B (B1 and B2). The geometrical size of the samples was 37 mm and 60 mm in diameter and length, respectively. The measurements were made both under ambient pressure and under a confining pressure of 240 bars.

To address the potential for gas slippage effects, which can skew permeability measurements, we implemented the Klinkenberg correction on our collected data. This correction ensured that the data accurately represented the actual permeability of the samples. The outcomes of these tests were then averaged for each sample set to determine the average porosity and permeability characteristics of the formation under study. The findings from this phase provided essential preliminary insights into the behavior of the samples, informing our subsequent μ-CT investigations.

2.3. Micro-CT Imaging

Our imaging approach was designed to provide a resolution-specific characterization of pores in the DG sandstones A and B. A compromise between sample size and spatial resolution was inevitable as is always the case for X-ray microtomography studies. We detail the different imaging resolutions and respective sample dimensions used in this study.

Initially, to gain a general overview of the pore structures, we used the YXlon FF35 dual-tube μ-CT device at the University of Miskolc, Hungary. With its micro-focus X-ray source and a sensor size of 2176 × 1792 pixels, this equipment allowed us to scan the samples at a 5 μm resolution. For these scans, we prepared samples from categories A and B, reducing their diameters to about 8 mm (Figure 2) through precise coring.
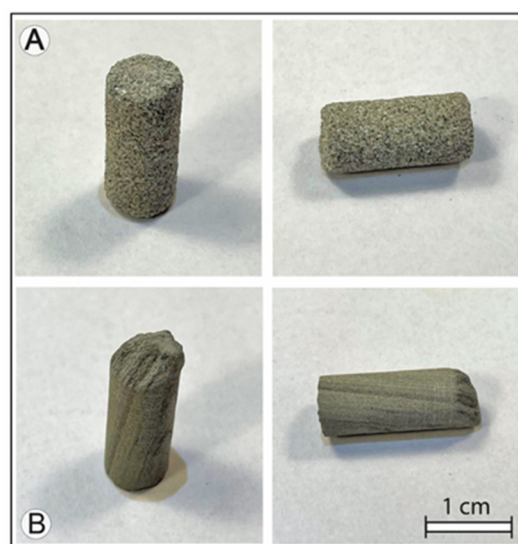
Figure 2. Sandstone core samples (**A**,**B**) prepared for 5 μm resolution scanning, with the coarseness (**A**) and layered texture (**B**) evident beside a scale bar for size reference.

To capture more detailed pore structures, we subsequently reduced the sample dimensions further to approximately 5 mm. This size was optimal for employing the nanotom M 180 system (Waygate Technologies, a Baker Hughes Company) at the Leibniz Institute for Applied Geophysics (LIAG), Germany, which facilitated scanning at 2 μm voxel sizes.

For the most detailed analysis, we scaled down the samples to approximately 3 mm and utilized the same nanotom M 180 system for 1 μm resolution scans. This highest resolution was chosen in accordance with the equipment's capability, which marks 1 μm as the limit of its resolution range.

All the scanning processes followed the methodologies established by Halisch and Schmitt [29,30], ensuring data acquisition precision and reliability. This detailed μ-CT imaging strategy, marked by gradual reductions in sample size and increases in resolution, was important in the comprehensive analysis of the internal structures of the DG sandstone samples.

By integrating these high-resolution μ-CT imaging results with the lab porosity and permeability measurements, our study introduces a methodology that has not been used in geothermal reservoir exploration in the study area. This combination offers an enriched and comprehensive assessment of the rock's physical properties, surpassing the capabilities of each method or resolution when used independently. Such integration is particularly significant in the field of geothermal reservoir characterization and management, setting a new benchmark for future studies.

However, it is important to acknowledge the obvious limitations and assumptions associated with our methodology. The sample size constraint due to μ-CT imaging resolution may not fully represent the heterogeneous nature of larger DG, a necessary compromise for efficient scanning and analysis across three resolutions for each sample. Additionally, there is an assumption that μ-CT imaging accurately captures all pore structures, which may not be true for samples with extremely fine or complex networks. Differences in scale and measurement principles between laboratory helium porosity, permeability measurements, and μ-CT imaging results might also affect our study's conclusions. To address these concerns, we carefully selected Sample A and Sample B for their representativeness of the broader geological spectrum within the DG. This approach enhances the reliability of extrapolating our findings to the broader geological formations, balancing the need for detailed analysis with practical constraints in sample size and resolution.

2.4. Imaging Analysis and Resolution Impact Assessment

Upon acquisition, the μ-CT images of the sandstone samples underwent advanced 3D visualization and analysis using AVIZO PerGeos Software Version: 2022.3 [31]. This software enabled us to employ previous methodologies as outlined by Halisch, Schmitt, and Ishutov [30,32,33], which included the application of thresholding and segmentation algorithms. These processes were crucial in analyzing the pore network in great detail, enabling us to comprehensively evaluate the pore size distribution at high resolution.

For each dataset of the 16-bit grayscale images, a volume of interest was chosen and then segmented into binary images to calculate the connected porosity as well as PSD for each subsample. Segmentation, a critical step in image analysis, directly influences all subsequent results [34]. While various methods exist for segmentation [35–37], in this study, we employed careful interactive threshold settings for each dataset, guided by the respective intensity histograms.

Incorporating this comparative analysis was a crucial element of our research, setting it apart from conventional applications of μ-CT imaging in geological studies. By carefully examining the pore structures at multiple resolutions, specifically 2 μm and 1 μm, we were able to discern how resolution choices influence the accuracy and reliability of pore structure analyses. This methodical examination is particularly new in the context of the DG and the Pannonian Basin. Our study goes beyond the standard use of μ-CT imaging, adopting a tailored approach that further integrates the high-resolution μ-CT imaging with the lab porosity and permeability measurements.

3. Results and Discussion

3.1. Helium Porosity and Permeability Results

We present a detailed breakdown of total porosity, pressure-specific porosity, and permeability both before and after the Klinkenberg correction in Table 1. These results provide foundational data for understanding the fluid flow potential of the samples under study as well as the general expected porosity and permeability for the studied samples.

Table 1. Results of helium porosity and Klinkenberg-corrected permeability for DG replica samples A and B.

Sample #	φ [%]	Φ_{Pressure} [%]	K_{gas} [mD]	K_{Kl} [mD]
A_1	30.56	27.81	449	388
A_2	31.7	28.39	633	557
A (average)	31.13	28.1	541	472.5
B_1	8.24	6.32	0.05	0.01
B_2	15.61	12.17	0.04	0.01
B (average)	11.925	9.245	0.045	0.01

The results indicate a notable distinction between the two samples, which can be attributed to differences in their grain size and cementation patterns. Specifically, Sample A, characterized by coarser grain size and less extensive cementation, exhibited significantly higher porosity and permeability, >30% and ~400 mD, respectively, as compared to the low porosity and permeability, <15% and ~0.01 mD, respectively, observed in Sample B. This suggests that Sample A may have a good fluid flow potential, which is a critical component in the performance of geothermal reservoirs. The observed variations in Klinkenberg-corrected permeability further emphasize the influence of pore structure and connectivity on fluid transport within these formations.

The observed low porosity and permeability in Sample B are indicative of its limited suitability for use as a geothermal reservoir. This sample's fine-grained texture is linked to lower porosity, likely due to a reduction in interconnected pore spaces or the presence of isolated pores. Furthermore, the porosity measured may also reflect the presence of fissures or stratifications introduced during sediment deposition. These factors are crucial in our μ-CT imaging analysis, as they influence the interpretation of porosity and permeability relevant to geothermal potential.

3.2. Micro-CT Imaging Results

μ-CT imaging at various resolutions allowed for the visualization and quantification of the internal microstructures of the DG sandstone samples, with a particular focus on their pore networks. The 5 μm resolution scans did not reveal clear details for the two samples, presenting grainy images, as depicted in Figure 3. The only discernible feature was a fracture in Sample B. Beam hardening, an imaging artifact described by Ketcham and Carlson [38] caused by X-rays being preferentially absorbed by denser materials leading to bright rings at the edges of the samples, is evident in the raw images captured in Figure 3. These artifacts, especially prominent in the 2 μm and 1 μm resolution scans, needed to be removed before undertaking any image segmentation. Particularly for Type B, the μ-CT imaging at 1 μm and 2 μm resolutions failed to resolve the finer porosity details effectively due to the sandstone's dense composition and low porosity, emphasizing the need for higher imaging resolution.
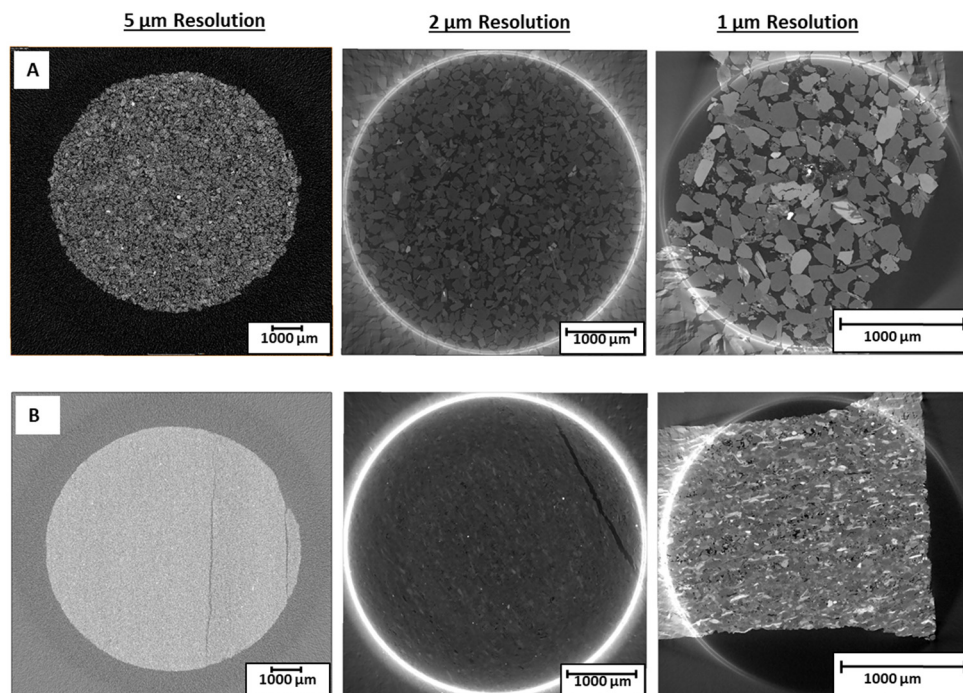
Figure 3. μ-CT 2D slices of uncropped 16-bit grayscale images at 5, 2, and 1 μm resolutions from left to right, respectively. The top set of images corresponds to Sample (**A**), and the bottom set to Sample (**B**) as indicated. A fracture can be observed in Sample (**A**).

Due to the necessity to eliminate imaging artifacts and surrounding void, the image processing and cropping of the data to derive a representative region of interest was performed. This is shown in Figures 4 and 5 for samples A and B, respectively, and includes all the resolutions used. Additionally, each cropped image is accompanied by an intensity histogram to provide further insight into the data. The structures in 5 μm resolution images were not further investigated due to their limited details and noise.
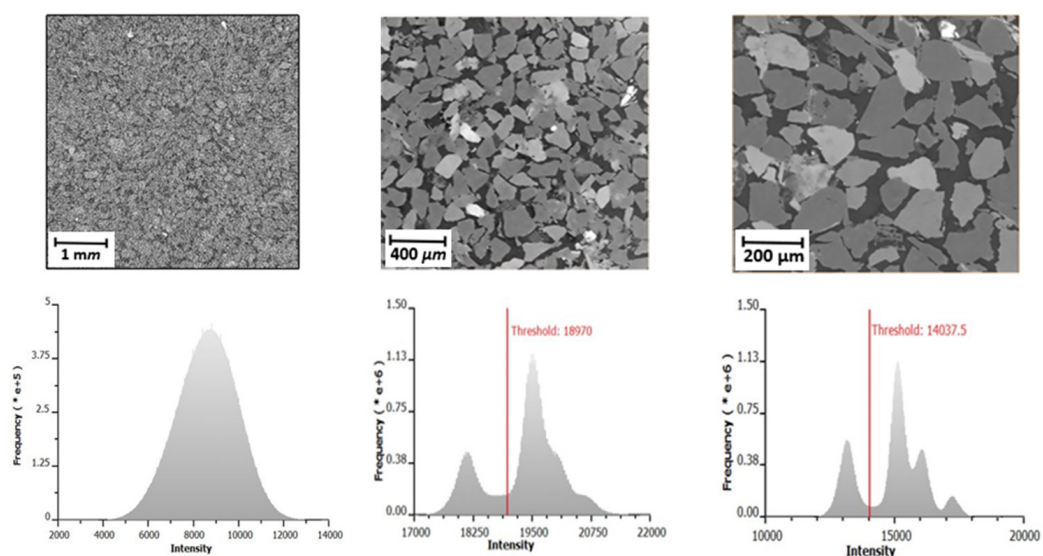
Figure 4. The 2D slices of sandstone rock Sample A at resolutions of 5 μm, 2 μm, and 1 μm, from left to right displayed as 16-bit grayscale images. The grayscale histograms beneath the according image reveal the distribution of 16-bit grayscale values. The thresholds were determined using the interactive thresholding capabilities of Avizo software, guided by the intensity histograms of the respective datasets. Multiple iterations were executed to refine the boundary between the void and grains.
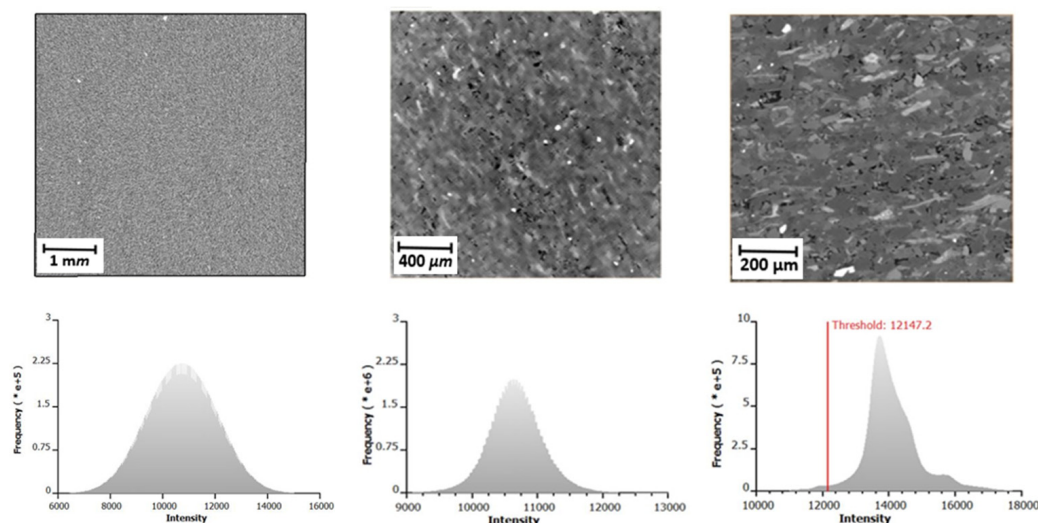
Figure 5. The 2D slices of sandstone rock Sample B at resolutions of 5 μm, 2 μm, and 1 μm, from left to right displayed as 16-bit grayscale images. The grayscale histograms beneath the according image reveal the distribution of 16-bit grayscale values. Similar to Figure 4, the thresholds were determined using Avizo software, relying on user-defined grayscale values and guided by the intensity histograms. Multiple iterations were necessary to ensure accurate segmentation, particularly for data with underdeveloped peaks in the histograms.

Figures 4 and 5 showcase cropped 2D slices of the samples at 5 μm, 2 μm, and 1 μm resolution, revealing the intricate microstructures of the DG sandstones. These images highlight the contrast between different phases within the samples, indicative of variations in mineral composition and density. In the grayscale images, the darkest areas represent the pore spaces, while the spectrum from dark gray to white corresponds to the varying densities of grains and minerals, as noted by Vaz [39]. Both the medium-grained Sample A and fine-grained Sample B display these dark pore regions; however, in B, the pores are fewer and smaller in size. Segmentation was subsequently employed to isolate the pores for detailed analysis.

Segmentation and Pore Space Analysis at Different Resolutions

Segmentation in μ-CT data analysis is a fundamental step that delineates different phases within the rock, such as pore spaces and mineral grains. This study utilized the interactive thresholding capabilities of Avizo PerGeos software Version: 2022.3 [31], which allowed us to isolate the void phase by carefully selecting a user-defined grayscale threshold value. This choice of the threshold value was user-defined and required the separation of the voids from the rest of the rock as our region of interest. This task relied purely on the operator's discernment with guidance from the intensity histograms of the respective dataset. This is especially crucial when the intensity histograms lack distinct peaks or show only underdeveloped peaks, a challenge we encountered with Sample B mostly at the 2 μm and partially at 1 μm resolution. To solve this, multiple iterations were executed to refine the region of interest with the utmost accuracy.

In our study, the "separate objects algorithm" was utilized to distinguish and analyze individual pores within the μ-CT datasets. This algorithm, integral to image processing, works by identifying and segmenting connected pixel clusters within the image that represent unique structures—such as pore spaces—based on their grayscale values. Once identified, these segments are treated as separate entities, allowing for detailed analysis of each pore's geometric and spatial characteristics. This segmentation process is necessary for accurate porosity quantification and was performed using Avizo software [31]. We then normalized pore sizes against the total porosity to ascertain the most impactful pore size contributing to overall porosity, an approach aligning with [30] Schmitt [30]. This nor-

malization addresses common misinterpretations associated with traditional frequency or count plots, which often overemphasize the abundance of smaller pores without accounting for their relative insignificance in total porosity contribution.

Moreover, permeability simulations were conducted for the highest resolution samples to estimate their permeability characteristics, though this attempt failed for Sample B, suggesting negligible permeability. Figures 6 and 7 visually illustrate these findings, showcasing 2D slices of each dataset with separated pores (colors are used to show the separation of adjacent pores without any relation to pore size); also shown is the frequency of pore sizes as well as the normalized pore size distribution all in that order. Table 2 complements this visualization by summarizing the μ-CT analysis and including these observations against the averaged helium porosity and permeability results for both samples.
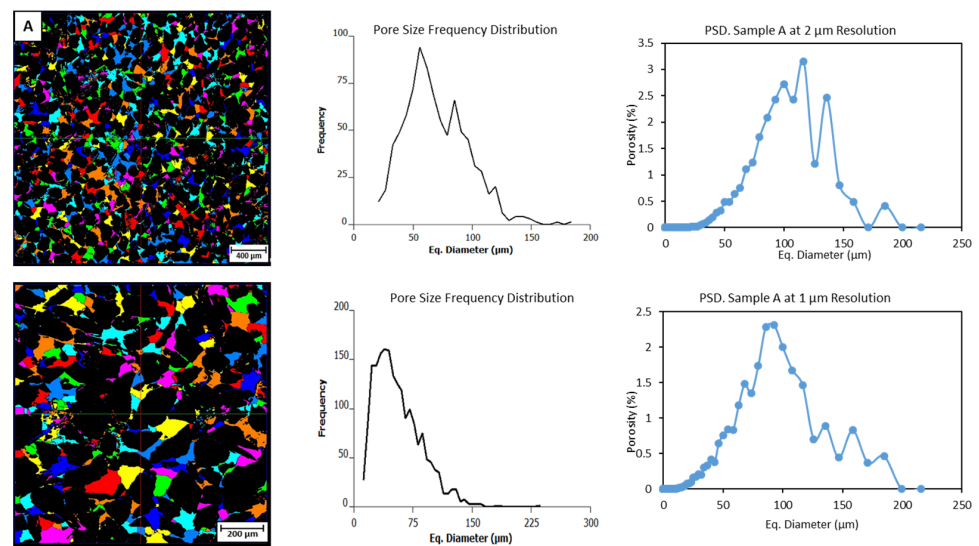
Figure 6. Pore space representation of A at 2 μm and 1 μm resolution in the top and bottom images, respectively; colors are used to solely differentiate between individual pores, and they have no correlation to the sizes of the pores. At the center is the pore size frequency distribution, and on the right, the pore size distribution with volume fraction for each resolution is shown.
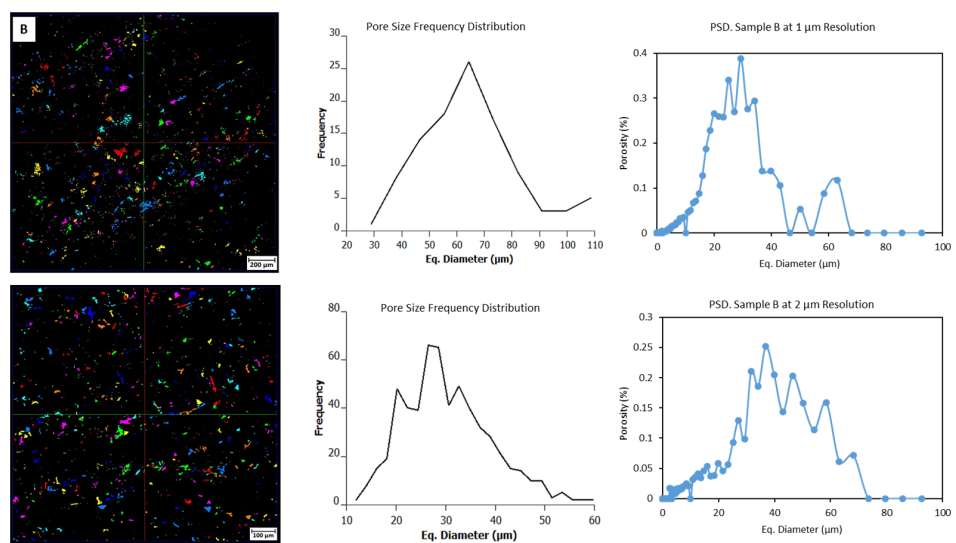
Figure 7. Pore space representation of B at 2 μm and 1 μm resolution in the top and bottom images, respectively; colors are used to solely differentiate between individual pores, and they have no correlation to the sizes of the pores. At the center is the pore size frequency distribution, and on the right, the pore size distribution with volume fraction for each resolution is shown.

Table 2. Comparison of parameters analyzed from lab (gas) measurements and 1 μm and 2 μm resolutions.

Sample ID #	Method	k (mD)	φ [%] Connected	Freq. Dependent Pore Size (μm)	Weighted Pore Size Mode (μm)	Pore Size Range (μm)
A	Gas	472.5	31.13	N/A	N/A	N/A
	1 μm	1800	25.0	100–120	50–60	1.5–190
	2 μm	NP	25.9	80–100	50–60	2.5–240
B	Gas	0.01	11.93	N/A	N/A	N/A
	1 μm	Failed	4.15	30–40	25–30	1.5–124
	2 μm	NP	2.8	25–35	60–70	2.5–76

Sample A: 2 μm Resolution Analysis: The 2 μm resolution scans for Sample A were analyzed to identify and quantify the pore space distribution. The frequency distribution (Figure 6, left graph) revealed a predominant pore size range, peaking at approximately 50–60 μm, suggesting a high occurrence of pores within this size bracket. However, the pore size distribution (PSD) (Figure 6, right graph) provided insight into the functional porosity, showing a notable peak in the 100–120 μm range. This indicates that medium- to large-sized pores (100–120 μm), despite being less frequent as compared to the 50–60 μm pores, play a dominant role in the porosity of the sample due to their substantial individual volumes.

Sample A: 1 μm Resolution Analysis: Upon examining the 1 μm resolution images, the frequency distribution maintained a similar pattern to that of the 2 μm resolution, reinforcing the consistency of the pore size distribution across the increased resolution (Figure 6, left graph). The mode pore size recorded ~60 μm is comparable to the 50–60 μm recorded under 2 μm resolution. The PSD for the 1 μm resolution (Figure 6, right graph) also presented a prominent peak within the most effective pore size range of 80–100 μm, aligning with the findings at 2 μm resolution. This consistency confirms the critical contribution of medium- to large-sized pores to the overall porosity and potential fluid flow within the sample.

The analysis of Sample A across both resolutions shows the important influence of medium-sized pores on porosity compared to the abundant smaller pores. Larger pores, while crucial for fluid transport, are less frequent and may be isolated, reducing their impact on flow dynamics. The frequency curves show the small pores to be the majority, but in reality, they seem to have minimal contribution to the total porosity, as evident in the normalized pore size distribution. Considering these observations, the two resolutions give satisfactory results, showing that this sample can be studied under both the 1 μm and 2 μm resolutions. The results also highlight the importance of considering pore volume in addition to frequency when evaluating porosity and permeability for geothermal energy exploration.

Sample B: 2 μm Resolution Analysis: At the 2 μm resolution, the frequency distribution graph for Sample B (Figure 7) indicates a concentration of pores with a diameter of around 60–70 μm, suggesting a dominance of this pore size within the sample. For this sample, the number of pores detected is relatively low. The normalized pore size graph reveals a significant porosity contribution from smaller pores, specifically in the range of 25–35 μm, as well as a contribution from a different group of pores about 60 μm. This observation highlights the role that small to medium-sized pores play in the porosity of this sample, which is critical for assessing the sample's potential for fluid transport.

Sample B: 1 μm Resolution Analysis: When examined at the 1 μm resolution, the frequency distribution becomes narrower, with a peak at around 25–30 μm, hence a slightly different pore size spectrum compared to what was observed at 2 μm. The normalized PSD shows that the highest porosity contribution comes from pores in the 30–40 μm range. This is different from the 60–70 μm range observed under 2 μm.

An important observation from the imaging is the limited number of pores identified in Sample B even at our finest resolution. Also, examining the 2D slice shown for this case,

it is evident that the pores seem to be linearly aligned, resembling features such as fissures or deposition lines, which might also manifest as cracks in larger sample sizes.

The 1 μm resolution analysis reveals that for Sample A, medium-sized pores predominantly contribute to the total porosity, suggesting effective fluid transport. However, for Sample B, the variation in contributing pore sizes, particularly the prominence of smaller pores, indicates a more complex pore structure. This complexity, coupled with less defined boundaries even at 1 μm resolution, suggests that a finer resolution might be necessary for a more accurate assessment of Sample B.

3.3. Comparative Analysis of Petrophysical Parameters

Table 2 presents petrophysical measurements across different methods: laboratory gas measurements and micro-CT imaging at 1 μm and 2 μm resolutions for Sample A and Sample B. "NP" (not performed) indicates that measurements were not executed due to resolution limitations and sample suitability, while "Failed" denotes experiments that were attempted but did not yield valid results due to technical challenges, especially with such dense material. Hence, "Failed" is interpreted as zero at this resolution.

In the comparative analysis between helium porosity and permeability tests and μ-CT imaging at 1 μm and 2 μm resolutions, as outlined in Table 2, there are notable differences in the interpretation of the sample characteristics. For Sample A, μ-CT imaging at 1 μm resolution suggests a significantly high permeability of 1800 mD, contrasting with the 472 mD recorded from nitrogen gas permeability measurements. While the Pannonian Basin, particularly the DG, has recorded permeability exceeding 2 Darcy in some areas, as reported by Koroncz and Toth and Almasi [12,25], the high permeability recorded for Sample A does not accurately represent the actual conditions of the studied sample. This may be a limitation of μ-CT imaging, considering its limited representativeness at such a microscale. We base our explanation on two more arguments; the sample was a medium- to coarse-grained sandstone and not from the highest permeability section, which, for DG, is categorized as coarse-grained with very poor cementation. Also, the lab-measured permeability on the larger sample showed lower permeability. The porosity values show a small but acceptable difference, with 31% recorded by helium pycnometry and approximately 25% by μ-CT imaging. This is an acceptable range considering the precision of helium gas porosity measurements and the larger sample investigated in the lab.

On the other hand, Sample B displays more consistent permeability across the two methods, with both gas permeability and μ-CT imaging indicating very low permeability, at 0.01 mD and 0 mD, respectively, a conclusion derived after the failed results. The porosity measurements, however, differ, showing approximately 11% for helium pycnometry and around 4% for μ-CT imaging. This discrepancy in porosity values can be attributed to the μ-CT imaging's limitations in detecting smaller, isolated pores in this finer-grained sample. Additionally, the μ-CT imaging process involved cropping out visible fractures before data analysis, which could also contribute to the differences observed. On the other hand, lab measurements were made on a larger sample that had visible depositional features, which are more likely to contribute to this porosity. These findings show the crucial role of integrating geological insights and corroborative laboratory data for a more accurate interpretation of μ-CT imaging results, particularly in geothermal energy exploration where understanding fluid transport characteristics is essential.

Novice researchers working with μ-CT should be keen to recognize the limitations of resolution in capturing complete pore structures and to be cautious about misinterpretations based on pore frequency alone. Higher resolutions are crucial for detailed analysis but may not always be necessary for all samples. Moreover, high resolution will always be a tradeoff between resolution and sample dimensions. Experienced CT users, on the other hand, should emphasize the integration of μ-CT data with geological context and other laboratory measurements, understanding that μ-CT results may require careful

interpretation to account for potential discrepancies in representativeness, especially in heterogeneous samples.

At 5 μm resolution, the images of the two samples exhibited a homogeneous phase distribution with blurred or indistinct pores, leading to a grainy texture in the images. The finer details essential for accurate pore structure analysis were concealed. Since the samples at hand contained large grains and large pores, especially Sample A, which could be imaged at a 5 μm resolution, we attribute these results to suboptimal scanning parameters, which led to poor signal-to-noise ratio. For this scan, filtering algorithms could not enhance the signal-to-noise ratio. This compromised image quality made the images unsuitable to define a threshold that could ensure image segmentation, thus highlighting the importance of optimal scan settings and resolution choice coupled with some background knowledge about the sample to be scanned.

4. Conclusions

The challenge in resolving structures at a 5 μm resolution highlights the need for optimal scanning parameters and careful resolution selection in μ-CT imaging.

For sample category A, effective analysis at 2 μm and 1 μm resolutions reveals high porosity and permeability, suggesting its suitability for geothermal applications. Nevertheless, additional comprehensive studies, including mineralogical analysis, are necessary to evaluate risks like clogging. Our results indicate that, for the DG, if a sample's pore structure is not clearly discernible at 2 μm resolution, it may not be suitable for geothermal exploitation, as evidenced by the low porosity and permeability in sample category B.

Sample category B, characterized by its compact nature and indistinct pore structures even at 1 μm resolution, demonstrates limited geothermal potential, underscoring the necessity for high-resolution imaging for accurate characterization. Moreover, our findings propose the following implication for geothermal reservoir assessment in the DG: If a sample's pore structure cannot be adequately resolved at a 1 μm resolution, it likely signifies exceedingly low permeability and small pore sizes. Such characteristics suggest that the region may not be favorable for geothermal exploitation due to the likely impediments in fluid transport. This additional criterion serves as a guideline in evaluating the feasibility of geothermal reservoirs in the region, contributing to a more efficient and sustainable exploitation of geothermal energy.

As previously mentioned, our study grouped sandstone samples into categories A and B based on their different geological characteristics, with one representative from each category selected for detailed analysis. Type B, chosen to represent denser, less permeable formations, represents a significant segment of geological environments within geothermal reservoirs. Despite its limited geothermal potential, the characteristics of Type B are representative of similar compact geological formations, demonstrating the relevance of our findings to wider geothermal studies. However, the insights into pore structure analysis and fluid dynamics developed in this study are applicable to other types of porous reservoirs, such as hydrocarbon reservoirs. The principles of porosity and permeability assessment from our research can improve the understanding and management of various subsurface reservoirs beyond the specific context of geothermal energy.

5. Outlook

The insights gained from this study lay a foundation for future explorations, particularly focusing on experimental setups to investigate physical clogging phenomena within the Pannonian Basin's geothermal reservoirs specifically using medium- to coarse-grained samples. This direction is essential for advancing geothermal exploitation techniques and ensuring the sustainable and efficient development of Hungary's geothermal energy resources.

References

1. Lund, J.W.; Freeston, D.H.; Boyd, T.L. Direct utilization of geothermal energy 2010 worldwide review. *Geothermics* **2011**, *40*, 40159–40180. [CrossRef]
2. Qin, J.; Rosenbauer, R.J.; Duan, Z. Experimental measurements of vapor-liquid equilibria of the $H_2O + CO_2 + CH_4$ ternary system. *J. Chem. Eng. Data* **2008**, *53*, 1246–1249. [CrossRef]
3. Ma, S.; Yang, Y.; Lei, X.; Yue, B. Water scaling predication for typical sandstone geothermal reservoirs in the Xi'an Depression. *Energy Geosci.* **2023**, *4*, 100182. [CrossRef]
4. Njeru, R.M.; Halisch, M.; Szanyi, J. Micro-scale investigation of the pore network of sandstone in the Pannonian Basin to improve geothermal energy development. *Geothermics*, 2024; *in press*. [CrossRef]
5. Hurter, S.; Schellschmidt, R. Atlas of geothermal resources in Europe. *Geothermics* **2003**, *32*, 779–787. [CrossRef]
6. Tulinius, H.; Ádám, L.; Halldórsdóttir, H.; Yu, G.; Strack, K.; Allegar, N.; He, L.; He, Z. Exploring for geothermal reservoirs using broadband 2-D MT and gravity in Hungary. *SEG Tech. Progr. Expand. Abstr.* **2008**, *27*, 1147–1151. [CrossRef]
7. Dövényi, P.; Horváth, F. A Review of Temperature, Thermal Conductivity, and Heat Flow Data for the Pannonian Basin. In *The Pannonian Basin: A Study in Basin Evolution*; American Association of Petroleum Geologists: McLean, VA, USA, 1988; Volume 45. [CrossRef]
8. Yu, G.; He, Z.X.; Hu, Z.Z.; Porbergsdottir, I.M.; Strack, K.M.; Tulinius, H. Geothermal exploration using MT and gravity techniques at Szentlo˝rinc area in Hungary. In *SEG Technical Program Expanded Abstracts 2009*; Society of Exploration Geophysicists: Houston, TX, USA, 2009; pp. 4333–4338. [CrossRef]
9. Nádor, A.; Kujbus, A.; Tóth, A.; Use, G.E. Country Update for Hungary. European Geothermal Congress 2019 Den Haag, 2019. Available online: www.mbfsz.gov.hu (accessed on 29 November 2023).
10. Willems, C.J.L.; Cheng, C.; Watson, S.M.; Minto, J.; Williams, A.; Walls, D.; Milsch, H.; Burnside, N.M.; Westaway, R. Permeability and mineralogy of the Újfalu formation, hungary, from production tests and experimental rock characterization: Implications for geothermal heat projects. *Energies* **2021**, *14*, 4332. [CrossRef]
11. Ungemach, P. Reinjection of cooled geothermal brines into sandstone reservoirs. *Geothermics* **2003**, *32*, 743–761. [CrossRef]
12. Töth, J.; Almasi, I. Interpretation of observed fluid potential patterns in a deep sedimentary basin under tectonic compression: Hungarian Great Plain, Pannonian Basin. *Geofluids* **2001**, *1*, 11–36. [CrossRef]
13. Békési, E.; Fokker, P.A.; Candela, T.; Szanyi, J.; van Wees, J.D. Ground motions induced by pore pressure changes at the Szentes geothermal area, SE Hungary. *Geotherm. Energy* **2022**, *10*, 3. [CrossRef]
14. Szijártó, M.; Vatai, Z.; Galsa, A. Numerical investigation of the groundwater age and heat transport processes in asymmetric hydrogeological situations. In Proceedings of the EGU General Assembly 2023, Vienna, Austria, 24–28 April 2023. EGU23-3840. [CrossRef]
15. Bakke, S.; Øren, P.-E. 3-D Pore-Scale Modelling of Sandstones and Flow Simulations in the Pore Networks. *SPE J.* **1997**, *2*, 136–149. [CrossRef]
16. Takase, A.; McNulty, T.; Fitzgibbons, T. Foam Porosity Calculation by X-Ray Computed Tomography and Errors Caused by Insufficient Resolution. *Microsc. Microanal.* **2018**, *24*, 546–547. [CrossRef]

17. Buday-Bódi, E.; Irfan, A.; McIntosh, R.W.; Fehér, Z.Z.; Csajbók, J.; Juhász, C.; Radócz, L.; Szilágyi, A.; Buday, T. Subregion-Scale Geothermal Delineation Based on Image Analysis Using Reflection Seismology and Well Data with an Outlook for Land Use. *Sustainability* **2022**, *14*, 3529. [CrossRef]
18. Munawar, M.J.; Lin, C.; Cnudde, V.; Bultreys, T.; Dong, C.; Zhang, X.; De Boever, W.; Zahid, M.A.; Wu, Y. Petrographic characterization to build an accurate rock model using micro-CT: Case study on low-permeable to tight turbidite sandstone from Eocene Shahejie Formation. *Micron* **2018**, *109*, 22–33. [CrossRef] [PubMed]
19. Xiong, T.; Chen, M.; Jin, Y.; Zhang, W.; Shao, H.; Wang, G.; Long, E.; Long, W. A New Multi-Scale Method to Evaluate the Porosity and MICP Curve for Digital Rock of Complex Reservoir. *Energies* **2023**, *16*, 7613. [CrossRef]
20. Li, Y.; Zhang, Z.; Wei, S.; Yang, P.; Shang, Y. Opportunities in measuring multiscale pore structure of the continental shale of the yanchang formation, ordos basin, china. *Energies* **2021**, *14*, 5282. [CrossRef]
21. Horvath, F.; Bodri, L.; Abstracr, P.O. Geothermics of Hungary and the Tectonophysics of the Pannonian Basin "Red Spot". In *Terrestrial Heat Flow in Europe*; Čermák, V., Rybach, L., Eds.; Springer: Berlin/Heidelberg, Germany, 1979. [CrossRef]
22. Kovačić, M.; Grizelj, A. Provenance of the Upper Miocene clastic material in the southwestern part of the Pannonian Basin. *Geol. Carpathica* **2006**, *57*, 495–510.
23. Bérczi, I. Preliminary Sedimentological Investigation of a Neogene Depression in the Great Hungarian Plain. In *The Pannonian Basin: A Study in Basin Evolution*; American Association of Petroleum Geologists: McLean, VA, USA, 1988; Volume 45. [CrossRef]
24. Sztanó, O.; Szafián, P.; Magyar, I.; Horányi, A.; Bada, G.; Hughes, D.W.; Hoyer, D.L.; Wallis, R.J. Aggradation and progradation controlled clinothems and deep-water sand delivery model in the Neogene lake pannon, Makó Trough, Pannonian Basin, SE Hungary. *Glob. Planet. Chang.* **2013**, *103*, 149–167. [CrossRef]
25. Koroncz, P.; Vizhányó, Z.; Farkas, M.P.; Kuncz, M.; Ács, P.; Kocsis, G.; Mucsi, P.; Szász, A.F.; Fedor, F.; Kovács, J. Experimental Rock Characterisation of Upper Pannonian Sandstones from Szentes Geothermal Field, Hungary. *Energies* **2022**, *15*, 9136. [CrossRef]
26. Bálint, A.; Szanyi, J. A half century of reservoir property changes in the Szentes geothermal field, Hungary. *Cent. Eur. Geol.* **2015**, *58*, 28–49. [CrossRef]
27. Almási, I. Petroleum Hydrogeology of the Great Hungarian Plain, Eastern Pannonian Basin, Hungary. University of Alberta, 2001. Available online: https://www.nlc-bnc.ca/obj/s4/f2/dsk3/ftp04/NQ60365.pdf (accessed on 16 January 2024).
28. API. Recommended Practices for Core Analysis. 1998. Available online: https://www.energistics.org/sites/default/files/2022-1 0/rp40.pdf (accessed on 16 January 2024).
29. Halisch, M.; Steeb, H.; Henkel, S.; Krawczyk, C.M. Pore-scale tomography and imaging: Applications, techniques and recommended practice. *Solid Earth* **2016**, *7*, 1141–1143. [CrossRef]
30. Rahner, M.S.; Halisch, M.; Fernandes, C.P.; Weller, A.; dos Santos, V.S.S. Sampaio Santiago dos Santos, 'Fractal dimensions of pore spaces in unconventional reservoir rocks using X-ray nano- and micro-computed tomography. *J. Nat. Gas Sci. Eng.* **2018**, *55*, 298–311. [CrossRef]
31. Avizo Software Users Guide 2019. Available online: https://www.fei.com/software/avizo-user-guide (accessed on 16 January 2024).
32. Schmitt, M.; Halisch, M.; Muller, C.; Fernandes, C.P. Classification and quantification of pore shapes in sandstone reservoir rocks with 3-D X-ray micro-computed tomography. *Solid Earth* **2016**, *7*, 285–300. [CrossRef]
33. Ishutov, S.; Hasiuk, F.J.; Fullmer, S.M.; Buono, A.S.; Gray, J.N.; Harding, C. Resurrection of a reservoir sandstone from tomographic data using three-dimensional printing. *AAPG Bull.* **2017**, *101*, 1425–1443. [CrossRef]
34. Iassonov, P.; Gebrenegus, T.; Tuller, M. Segmentation of X-ray computed tomography images of porous materials: A crucial step for characterization and quantitative analysis of pore structures. *Water Resour. Res.* **2009**, *45*. [CrossRef]
35. Abera, K.A.; Manahiloh, K.N.; Nejad, M.M. The effectiveness of global thresholding techniques in segmenting two-phase porous media. *Constr. Build. Mater.* **2017**, *142*, 256–267. [CrossRef]
36. Nagata, R.; Reis, P.J.D.; Appoloni, C.R. Multi-scale approach to assess total porosity and pore size in four different kinds of carbonate rocks. *Micron* **2023**, *164*, 103385. [CrossRef]
37. Sezgin, B. Sankur, 'Survey over image thresholding techniques and quantitative performance evaluation. *J. Electron. Imaging* **2004**, *13*, 146. [CrossRef]
38. Ketcham, R.A.; Carlson, W.D. Acquisition, optimization and interpretation of X-ray computed tomographic imagery: Applications to the geosciences. *Comput. Geosci.* **2001**, *27*, 381–400. [CrossRef]
39. Vaz, C.M.P.; de Maria, I.C.; Lasso, P.O.; Tuller, M. Evaluation of an Advanced Benchtop Micro-Computed Tomography System for Quantifying Porosities and Pore-Size Distributions of Two Brazilian Oxisols. *Soil Sci. Soc. Am. J.* **2011**, *75*, 832–841. [CrossRef]